DECOMPOSITION OF MARTENSITE BY DISCONTINUOUS-LIKE PRECIPITATION REACTION IN AN Fe–17Cr–0.5C ALLOY

D. V. SHTANSKY†‡, K. NAKAI and Y. OHMORI

Department of Materials Science and Engineering, Faculty of Engineering, Ehime University, 3 Bunkyo-cho, Matsuyama 790-8577, Japan

Abstract—The mechanism of martensite decomposition and the kinetics of carbide precipitation have been studied in an Fe–17 wt% Cr–0.55 wt% C alloy. The morphology of carbide precipitates formed within the decomposed regions and the crystallography of their formation were examined by means of transmission electron microscopy after tempering at 735°C for various times. The martensite decomposition starts within less than 10 s, but it is not completed even after 10 min. The reaction initiates with the nucleation of fine cementite particles preferentially at the prior austenite grain boundaries and occasionally at the martensite lath boundaries. Cementite particles are related to the ferritic matrix with the Bagaryatsky orientation relationship. The decomposition of martensite proceeds heterogeneously by the migration of a reaction front. Various carbide morphologies were observed in the region close to the reaction front: rod-like, spherical or lamellae. The kinetics of martensite decomposition changes from carbon diffusion controlled to chromium diffusion controlled. After long time tempering, the alloy carbides, $M_{23}C_6$ and M_7C_3, precipitate at the reaction front. The $M_{23}C_6$ carbides are related with respect to the ferrite by the Kurdjumov–Sachs orientation relationship. Two specific orientation relationships were found between the M_7C_3 carbide and the ferrite, which are related to each other by a rotation of 30° about their common axis of $[0001]_h//[110]_\alpha$. One of them has previously been reported. The specific features of discontinuous-like precipitation in martensite are discussed and are attributed to the presence of carbon and chromium atoms, which have different mobilities. The driving forces for diffusion of carbon and chromium were qualitatively determined with the software and database ThermoCalc by assuming local equilibrium at the moving interfaces. © 2000 Acta Metallurgica Inc. Published by Elsevier Science Ltd. All rights reserved.

1. INTRODUCTION

Supersaturated martensite in an iron-based alloy is highly unstable and decomposes to ferrite and carbides during the subsequent tempering. This reaction may take various forms depending on the initial as-quenched state, temperature and the chemical composition.

Tempering of martensite in carbon steels has been studied extensively [1–23] and several distinct stages were identified: the segregation of carbon atoms to dislocations and various boundaries [2, 3], the rearrangement and the clustering of carbon atoms [4, 5] into a modulate structure [6, 7], the development of the transition carbides [8–15], the decomposition of retained austenite [16, 17], the replacement of transition carbides by cementite [18–21], the coarsening of fine martensite lath structure [22] and the formation of alloy carbides in low alloy steels [23].

The precipitation behavior in high alloy steels is also well known [24–39]. There have been many tempering studies on a variety of high Cr steels such as Cr [24–26], Cr–Mo [27–32], Cr–Mo–V [31, 33–38], high-chromium ferritic [39] and high-speed [40] steels. These results have shown various precipitation sequences with tempering temperature. In the last decade, attempts to predict the development of microstructural stages in various high alloy steels [30, 31, 35] have been made and the calculations appear to be in good agreement with the experimental results.

Tempering of the alloy steels induces a number

---

† On leave from the I. P. Bardin Iron and Steel Industry Institute, 2nd Baumanskaya Street, 9/23, Moscow 107005, Russia. Present address: Department of Materials Science, Faculty of Engineering, The University of Tokyo, 7-3-1 Hongo, Bunkyo-ku, Tokyo 113-8656, Japan.

‡ To whom all correspondence should be addressed.

of transient alloy carbides within the martensite laths, at lath boundaries and at prior austenite grain boundaries. These metastable carbides are replaced by more stable carbides. The coarsening of the lath boundary carbides, and the recovery and recrystallization of ferrite follow. Most researchers have noted that the distribution of carbides is extremely uniform between martensite laths and between prior austenite grains, these precipitates being located at lath and grain boundaries and within the matrix. Various mechanisms of carbide nucleation such as *in situ* nucleation within the pre-existing carbides and separate nucleation have been reported. Structural changes during tempering have mostly been studied in commercial steels rather than in high-purity Fe–Cr–C alloys, although the sequence of carbide precipitation was found to be very sensitive to the alloy composition [27, 30].

The orientation relationships (ORs) between the ferrite and various precipitates which form during tempering, and the change of the ferrite orientation during recrystallization are also very important to understand the crystallography of the reaction. The OR between cementite and ferrite has been studied for quenched and tempered specimens by a number of researchers [41–44]. The ORs between ferrite and alloy carbides such as $M_{23}C_6$ and M_7C_3 during tempering have been examined by Kuo and Jia [34] and Dyson and Andrews [45], respectively. However, the crystallographic relationships between all coexisting phases in high alloy steels during tempering have received less attention.

As described above, there are large differences in the kinetics of precipitation in various steels. Thus, in the present study, the decomposition mechanism of martensite at 735°C in a high purity Fe–17 wt% Cr–0.55 wt% C alloy which has not previously been reported in the literature has been examined by means of transmission electron microscopy. The experimental results are compared with the theoretical predictions using calculated phase diagrams.

2. EXPERIMENTAL PROCEDURE

The chemical composition of the alloy used in the present investigation is shown in Table 1. In order to avoid inhomogeneity in the initial structure, the carbon content of the alloy was selected such that the composition falls well within an austenite single-phase field at the solution temperature, ~1200°C, as in Fig. 1. However, the structural examination after the austenitization at 1200°C for 15 min showed that the large carbide particles were

not completely dissolved in austenite. Thus, a solution temperature as high as 1250°C was chosen.

Specimens $10 \times 10 \times 20 \text{ mm}^3$ were austenitized for 15 min in a dynamic argon atmosphere and then quenched into iced brine. Thin sheets $7 \times 7 \times 0.3 \text{ mm}^3$ were sliced from the center of each heat-treated specimen, tempered in a lead bath covered with a layer of active charcoal to prevent decarburization at 735°C for various times between 10 and 30 s, and then quenched into iced brine. For longer tempering times, bulk specimens of dimensions $7 \times 7 \times 10 \text{ mm}^3$ were encapsulated in evacuated quartz tubes, isothermally held at 735°C for various times between 5 min and 240 h, and quenched into iced brine.

After the heat treatments, the specimens were polished and etched using one of the following reagents depending on the phase composition: Villela's reagent (5 ml hydrochloric acid, 1 g picric acid in 100 ml of methanol), LePera's reagent (1 part of 1 ml sodium metabisulfite in 100 ml distilled water and 1 part of 4 ml picric acid in ethanol) or a solution of 1 g picric acid, 5 ml nitric acid and 100 ml ethanol. Thin foils for TEM studies were prepared from 3 mm discs, ground to a thickness of about 0.05 mm and electropolished by a conventional twin-jet polishing method using electrolyte containing 10% perchloric acid, 20% glycerol and 70% ethanol. The foils were examined in a JEM-3010 transmission electron microscope operating at 300 kV.

3. EXPERIMENTAL RESULTS

3.1. Optical microscopic observation
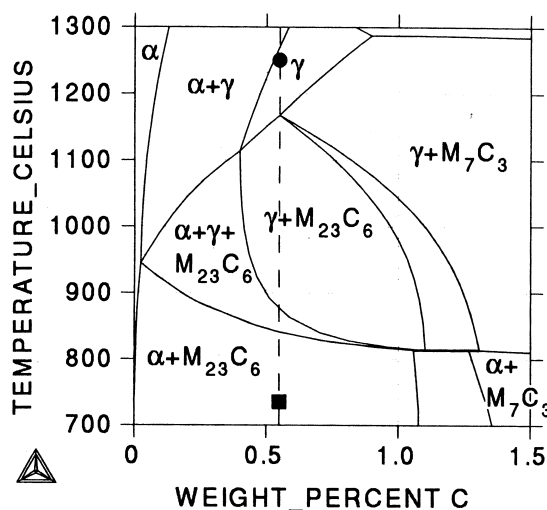
A typical optical micrograph showing the as-

Fig. 1. Calculated vertical section of the Fe–Cr–C system at 17 wt% Cr. The composition of alloy is marked by filled square.

Table 1. The chemical composition of the alloy (wt%)

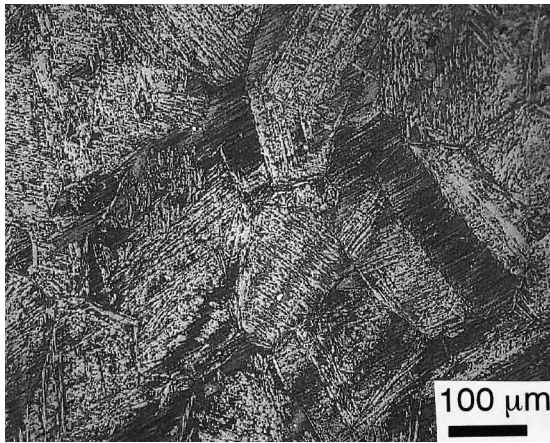| C	Si	Mn	P	S	Cr	Al	N	O
0.54	0.02	0.02	0.001	0.001	17.09	0.001	0.0036	0.002

Fig. 2. Optical micrograph for the specimen austenitized at 1250°C for 16 min and then quenched into iced brine.

quenched structure after the solution treatment at 1250°C for 16 min is presented in Fig. 2. The as-quenched structure was determined to be martensite with small amounts of retained austenite. Alloy carbides and δ-ferrite were not recognized. Transmission electron micrographs, Figs 3(a) and (b), show various shapes of the retained austenite such as thin continuous films between martensite laths, Fig. 3(a), and as three-dimensional grains enclosed by martensite laths with different habits, Fig. 3(b). High dislocation densities and stacking faults were frequently observed within the retained austenite. Analysis of the selected area electron diffraction (SAED) patterns revealed that the OR between austenite and martensite can be explained by either the Kurdjumov–Sachs [46] or the Nishiyama–Wasserman [47, 48] relationship. These observations are in good agreement with the results of Thomas and Rao [49, 50]. Figures 3(a) and (b) also demonstrate that there are no carbides in the as-quenched microstructure, i.e. no autotempering has occurred. Thus, it can be

thought that complete homogenization was achieved. These observations are in good agreement with the results of Irvine *et al.* [26] that chromium largely lowers the M_s temperature from 450°C for low-alloy steel to 300°C for 12% Cr steel.

Figures 4(a)–(e) show a set of optical micrographs, which illustrates the structural evolution with time at 735°C. It can be seen that the decomposition of martensite in the Fe–17Cr–0.55C alloy was unique compared with other steels so far investigated. The decomposition of martensite started at the prior austenite grain boundaries and this observation is in keeping with the previous results [29, 36]. Surprisingly, however, no decomposition within the prior austenite grains has occurred. Instead, the Widmanstätten-like morphology was observed. It can be seen in Fig. 4(a) that the Widmanstätten-like decomposition products of martensite nucleated either at prior austenite grain boundaries and grew into the parent austenite grains or nucleated directly within the grains. Subsequently, thick rims of martensite decomposition products were formed along the prior austenite grain boundaries. Figures 4(b) and (c) show how the reaction proceeded with increasing tempering time. The decomposition products gradually spread from the prior austenite grain boundaries into the matrix. It is important to note that, in the other parts of the prior austenite grains, any reaction was not observed. The decomposition of martensite was completed by tempering for less than 1 h but even after 5 h, Fig. 4(d), the packet morphology of martensite was clearly visible in keeping with the results by Caron and Krauss [22]. Figure 4(e) shows a typical example of the homogeneous distribution of $M_{23}C_6$ carbides within the ferrite matrix where the equilibrium state was nearly reached. Tempering for 240 h resulted in the poly-
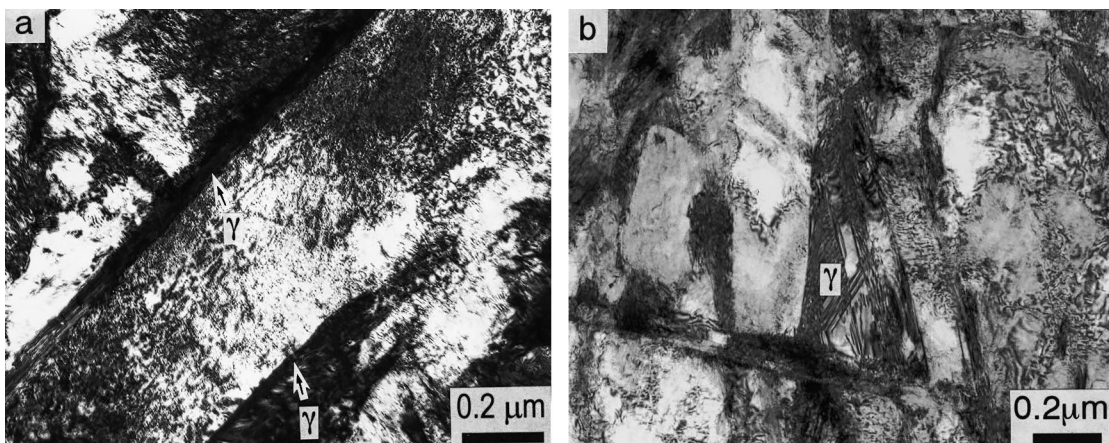

Fig. 3. TEM bright field micrographs of the as-quenched specimen showing morphology of retained austenite.

gonization of ferrite laths and coarsening of carbides.

3.2. TEM investigation

In order to clarify what happened in a high Cr martensite during tempering, a thorough TEM examination was done. Figure 5 shows a martensite lath that has completely decomposed into the mixture of ferrite and carbides after tempering for 10 s. The martensite lath contained the precipitates densely distributed. The adjacent martensite laths on both sides of this lath, however, remained undecomposed. Two carbide morphologies within the decomposed region can be distinguished: spherical shape with a diameter of 10–30 nm and rod-like
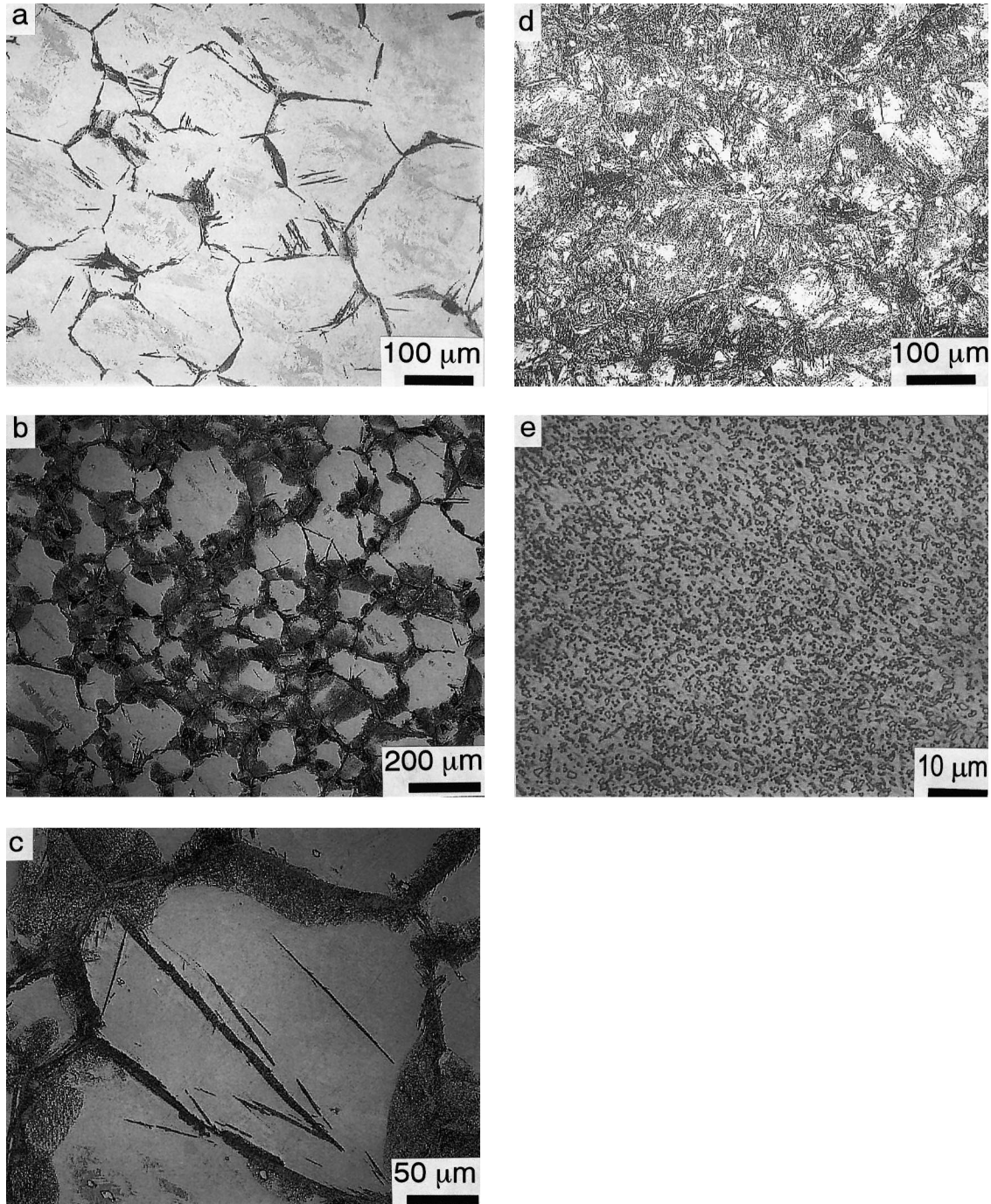

Fig. 4. Typical optical micrographs for specimens tempered at 735°C for various times: (a) 5 min; (b), (c) 10 min; (d) 5 h; (e) 240 h.

precipitates aligned in a specific direction with a length of 0.2–0.3 μm. Both of them were identified as cementite by the SAED patterns. It can be seen that the cementite particles in the patterns in Figs 5(b) and (c) were related to the ferrite by the variants of the Bagaryatsky OR:

$$(100)_\theta // (10\bar{1})_\alpha \quad (100)_\theta // (\bar{1}0\bar{1})_\alpha$$

$$(010)_\theta // (\bar{1}\bar{1}\bar{1})_\alpha \quad (010)_\theta // (11\bar{1})_\alpha$$

$$(001)_\theta // (\bar{1}2\bar{1})_\alpha \quad \text{and} \quad (001)_\theta // (1\bar{2}\bar{1})_\alpha.$$

Figure 6 shows the decomposition of martensite within a packet of martensite laths. It can be seen that the decomposed and the undecomposed regions formed alternately. The lath boundaries were even more densely populated by smaller precipitates (shown by arrows) in agreement with the previous results [29, 40]. The martensite laths within a packet are frequently twin related [51, 52]. Thus, from the results obtained, it is likely that the martensite decomposition reaction occurred preferentially within the laths, which have almost the same orientation.

Figure 7(a) shows the decomposition front in the specimen tempered at 735°C for 10 s. The SAED patterns from both the undecomposed, Fig. 7(b), and the decomposed regions, Fig. 7(c), show that the orientation of the matrix has not changed. Such an orientation behavior of the matrix was frequently observed at the decomposition fronts. Note that no SAED patterns obtained from the undecomposed martensite regions contained any carbide spots or streaks as observed in the tempered carbon steels [6]. Thus, no precipitation has occurred in the regions ahead of the reaction front.

Morphology and distribution of cementite particles in the decomposed regions after tempering for 10 s are illustrated in Fig. 8. Figure 8(a) shows the needle-like carbides aligned in specific directions. The length of needles was ∼50 nm. The cementite particles in Fig. 8(b) were distributed as some parallel rows, probably along the martensite twin boundaries. In this particular case the cementite particles precipitated with a common orientation. The precipitates in Fig. 8(c) grew as lamellae aligned in specific directions. Thus, the transformation is thought to proceed by a discontinuous-like precipitation reaction. In the right part of this micrograph
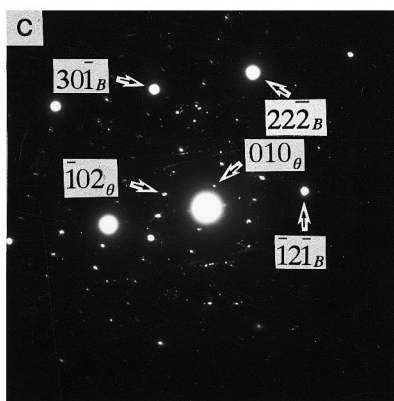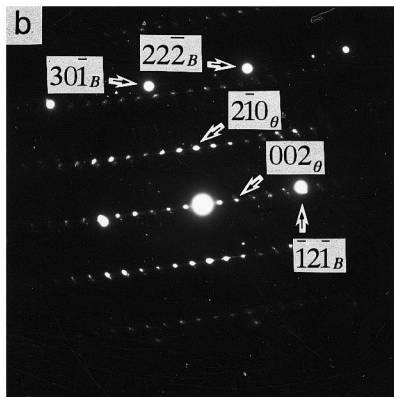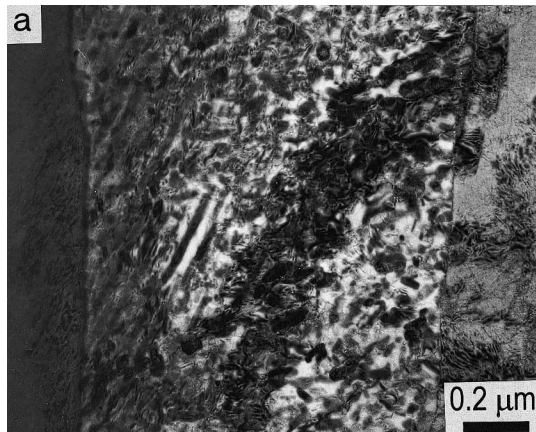

Fig. 5. TEM micrograph for the specimen tempered at 735°C for 10 s. (a) Bright field image for the decomposed structure of a martensite lath. (b), (c) SAED patterns from various decomposed regions within the lath showing two variants of the Bagaryatsky OR.
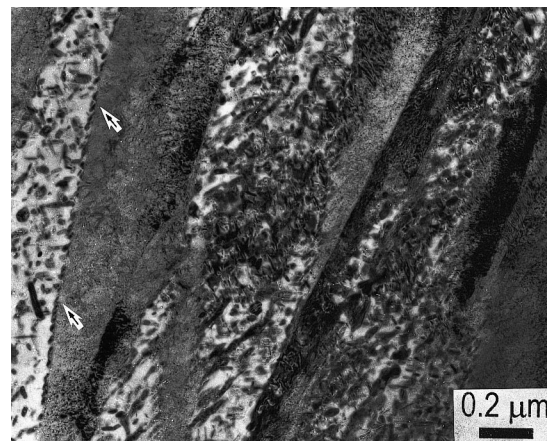
Fig. 6. TEM micrograph showing the heterogeneous decomposition of martensite laths within a packet in the specimen tempered at 735°C for 10 s.
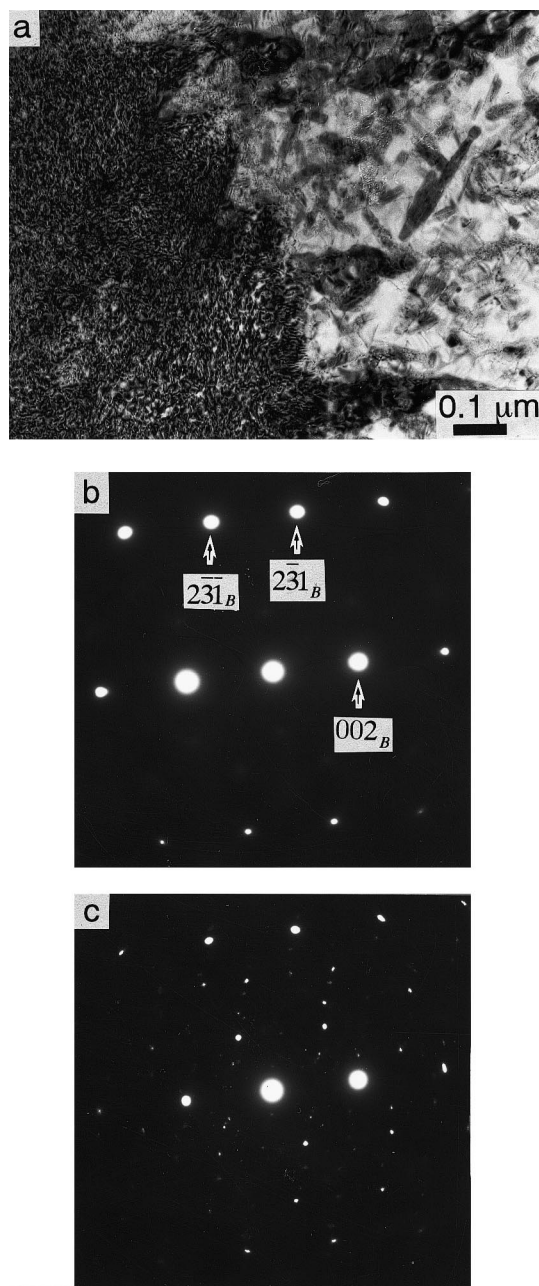
Fig. 7. TEM micrograph showing a front of transformation after tempering at 735°C for 10 s. (a) Bright field image. (b), (c) SAED patterns taken from the regions ahead and behind of the reaction front, respectively.

shown by an arrow in Fig. 9(a). It can be seen that two types of carbide, cementite and $M_{23}C_6$, had similar morphologies, and the shape of a precipitate cannot be a guide for its structure. This result agrees well with those of Beech and Warrington [24]. The stereographic analysis presented in Fig. 9(c) shows that the ferrite and the $M_{23}C_6$ carbide obeyed the Kurdjumov–Sachs OR. Note that the
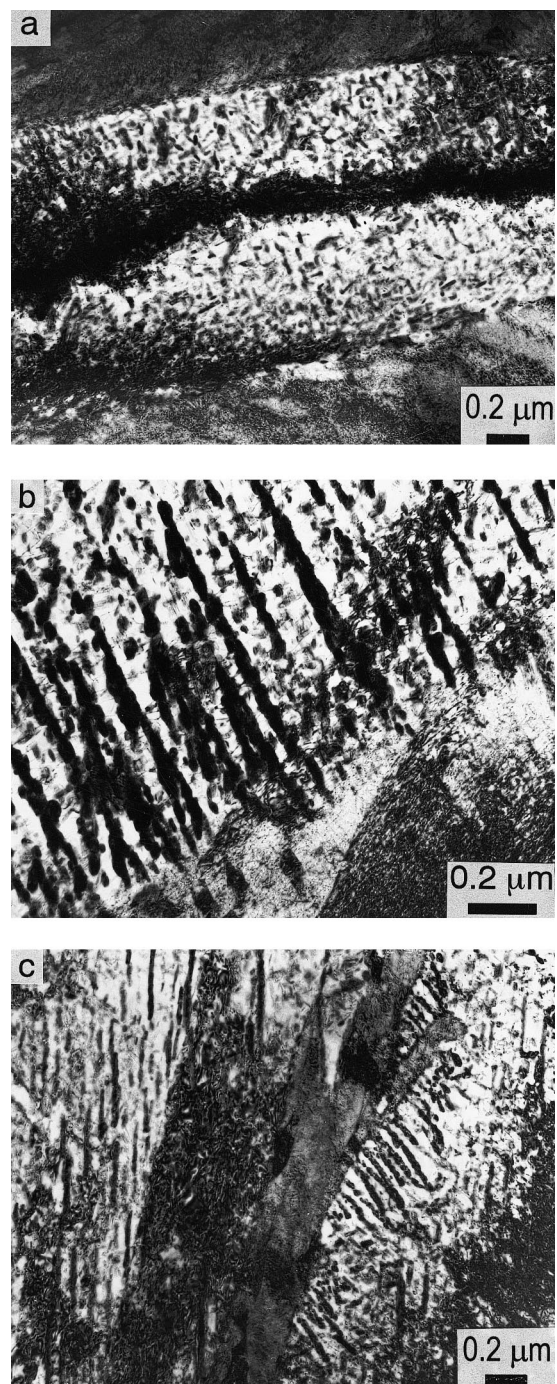
Fig. 8. TEM bright field micrographs showing morphology and distribution of the cementite particles after tempering at 735°C for 10 s.

the carbide lamellae were broken up into fine particles. In all cases presented in Fig. 8, the cementite precipitates were related to the ferritic matrix by the Bagaryatsky OR. Note that the OR reported by Pitsch and Schrader [53, 54] was never observed in the present study.

The $M_{23}C_6$ carbide was found to precipitate even at the beginning of tempering, probably concurrently with cementite at the reaction front. Figure 9(b) is the SAED pattern taken around the carbide

SAED pattern must be obtained from each single particle to determine the type of carbide.

It is important to note that all the reactions described above were definitely not the results of austenite decomposition but those of martensite. It can be seen in Fig. 10 that the reaction proceeded along an initial austenite grain boundary whereas the retained austenite was still stable both in the decomposed region of martensite and at a certain distance from it (shown by arrows).

Figure 11 shows the decomposition reaction in the vicinity of a prior austenite grain boundary. Figures 11(b)–(d) are the SAED patterns taken from various areas shown by arrows. The reaction proceeded preferentially along the prior austenite grain boundary. It should be noted that the reaction front migrated only into one of the prior austenite grains where the martensite laths exhibited almost the same orientations. No decomposition reaction can be recognized on the opposite side of the grain boundary. The fact that the orientation of the ferrite, which is the decomposition product of martensite, did not change from that of martensite agrees well with that reported above.

Figure 12 shows the middle part of the decomposed area presented in Fig. 11 after tilting 1.2°. Two ferrite orientations can clearly be recognized which are inherited from the parent twinned martensite crystals. Note that the rows of carbide particles aligned preferentially along the martensite twin boundaries.

The structure of specimens after tempering for 5 min showed a much greater variation in structure and morphology of precipitates. Figure 13(a) shows a pearlite-like structure in contact with an untransformed martensite. The carbide lamellae were identified as $M_{23}C_6$ bearing the Kurdjumov–Sachs OR with respect to the ferritic matrix [Fig. 13(c)]. Since the austenite has completely decomposed by tempering for 5 min, it is likely that this structure was formed from the retained austenite.

Figure 13(b) shows a degenerate pearlite-like
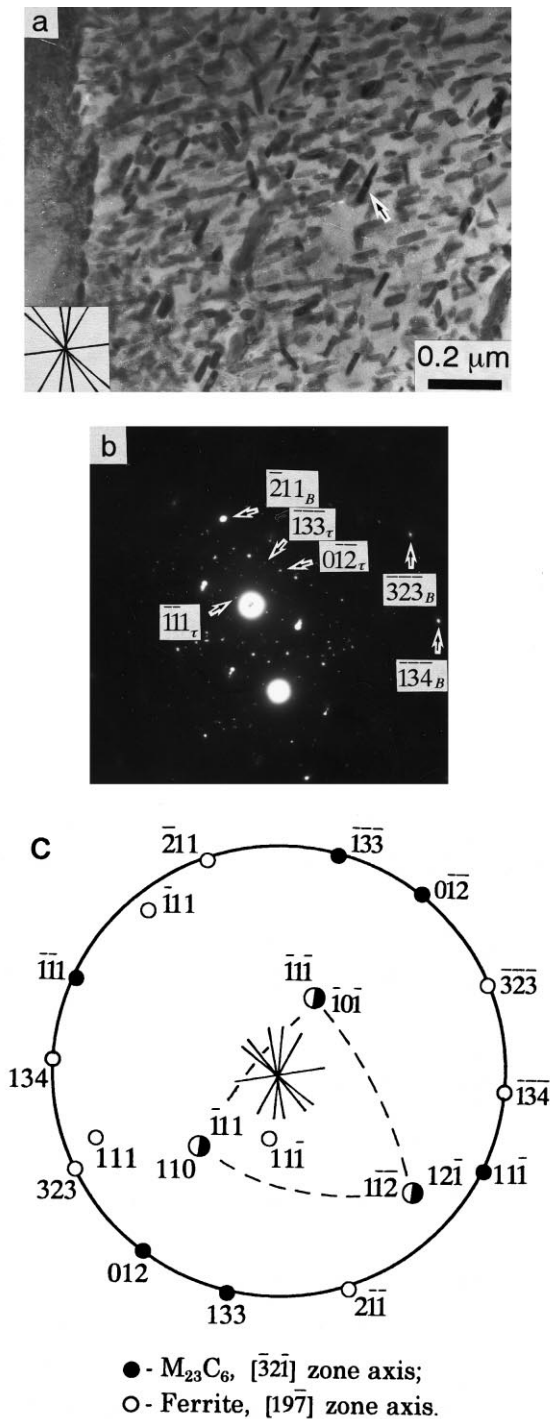
Fig. 9. TEM micrograph showing the $M_{23}C_6$ carbide precipitates within the decomposed region after tempering at 735°C for 10 s. (a) Bright field image, (b) SAED pattern taken around the particle shown by arrow and (c) its stereographic analysis.
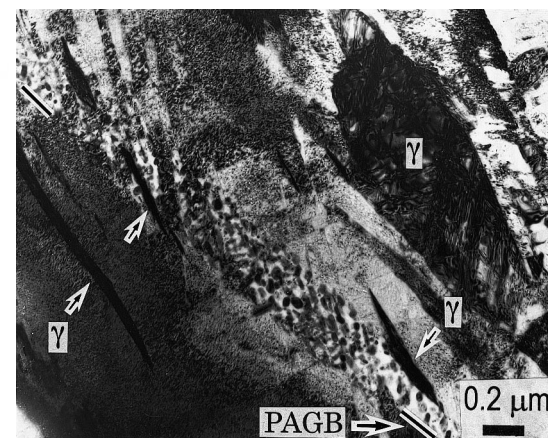
Fig. 10. Structure of the specimen after tempering at 735°C for 30 s. The retained austenite is shown by arrows. PAGB indicates the prior austenite grain boundary position.

structure that formed behind the reaction front. Note that the carbides were considerably larger than those observed after 10 s. Figure 13(d) is the SAED pattern taken from the particle shown in Fig. 13(b) by an arrow. This particle was identified as M_7C_3 and the OR between the ferrite and M_7C_3 carbide was deduced to be

$$\text{OR-I:} \quad \begin{aligned} (0001)_h &\approx //(1\bar{1}0)_\alpha \\ (01\bar{1}0)_h &\approx //(111)_\alpha \\ (2\bar{1}\bar{1}0)_h &\approx //(11\bar{2})_\alpha \end{aligned}$$

This OR is close to that reported by Dyson and Andrews [28].

Figure 14(a) shows small parallelogram-shaped
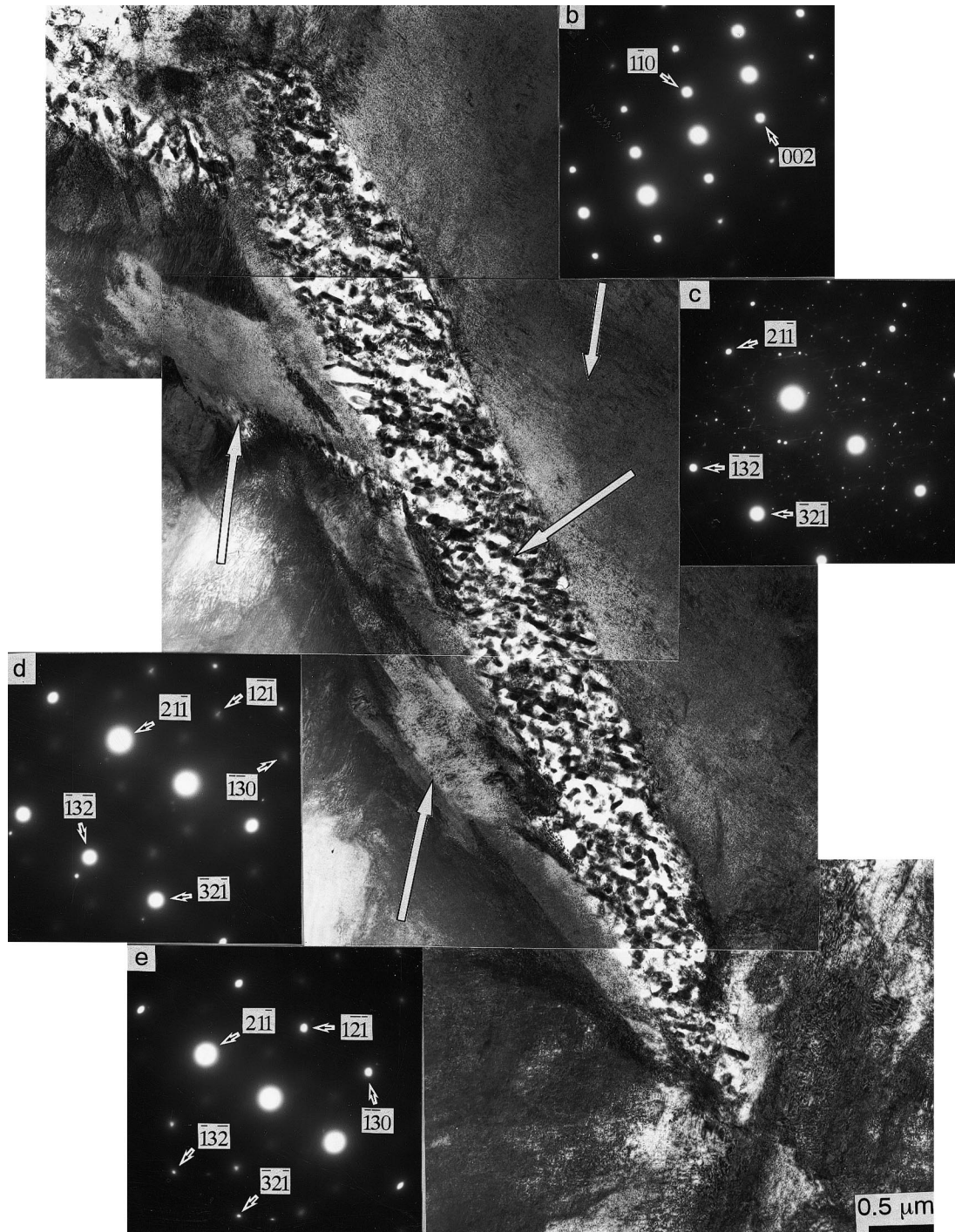
Fig. 11. TEM micrograph showing the decomposition of martensite along the initial austenite grain boundary. (a) Bright field image. (b)–(d) SAED patterns taken from various areas in (a).
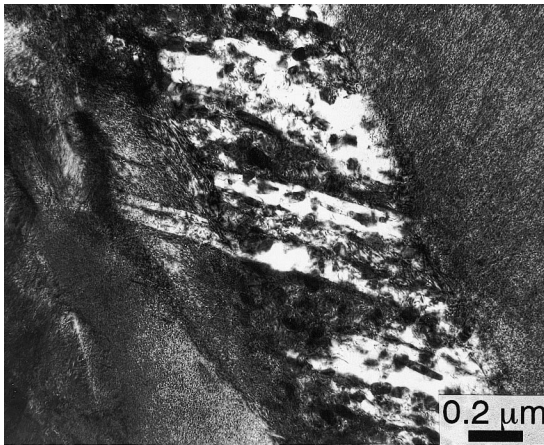
Fig. 12. TEM micrograph showing the ferrite inherited the twinned morphology of martensite in the specimen tempered at 735°C for 5 min.

precipitates, which were identified as M_7C_3. The SAED patterns taken from the different ferrite/carbide areas, Figs 14(b) and (c), allow their crystallography to be determined. The stereographic analysis for the SAED pattern in Fig. 14(b) is shown in Fig. 14(d). Note that these SAED patterns were taken for different zone axes, i.e. the orientation of the ferritic matrix was different. Thus, the following ORs between ferrite and M_7C_3 carbide were deduced:

new OR $\quad (0001)_h//(\bar{1}01)_\alpha \quad$ OR-I $\quad (0001)_h//(\bar{1}10)_\alpha$
$\qquad\quad (\bar{1}100)_h//(101)_\alpha \qquad\qquad (\bar{1}100)_h//(111)_\alpha$
$\qquad\quad (\bar{1}\bar{1}20)_h//(010)_\alpha \qquad\qquad (\bar{1}\bar{1}20)_h//(11\bar{2})_\alpha$

The OR-I is close to the Dyson and Andrews OR:

$(0001)_h//(011)_\alpha \quad (\bar{1}100)_h//(\bar{1}00)_\alpha \quad (11\bar{2}0)_h//(01\bar{1})_\alpha$.

The new OR has not been hitherto reported, but it is related by a rotation of 30° about the common axis $[0001]_h//[110]_\alpha$ with the OR-I reported by Dyson and Andrews [28].

After tempering for 1 h, only the $M_{23}C_6$ carbide particles were present. It was frequently observed that they were related to ferrite by the Kurdjumov–Sachs OR.

4. DISCUSSION

4.1. Summary of the experimental results

The experimental results described above can be summarized as follows:
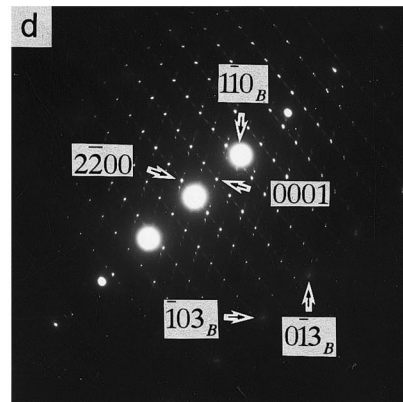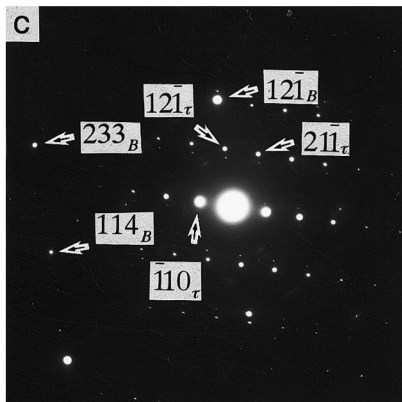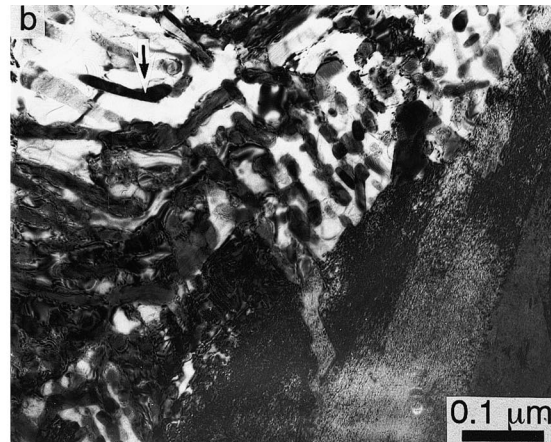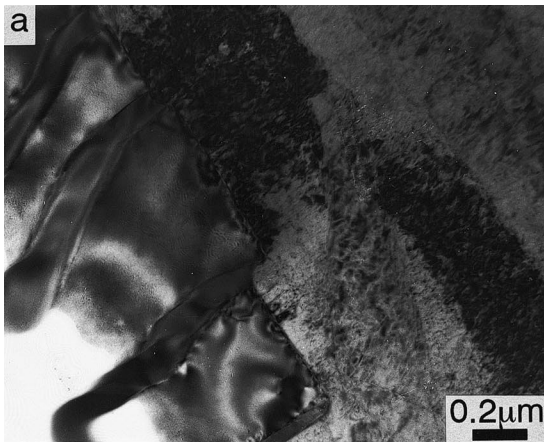
Fig. 13. The morphologies of alloy carbides after tempering at 735°C for 5 min. (a) $M_{23}C_6$ and (b) M_7C_3 carbide precipitates. (c), (d) Corresponding SAED patterns.

1. The martensite in the Fe–17Cr–0.55C alloy decomposed into ferrite and carbides inhomogeneously. The reaction classification will be given below.
2. The martensite decomposition started after tempering at 735°C within less than 10 s but was not completed even after 10 min.
3. The reaction started at the prior austenite grain boundaries and grew preferentially along these boundaries into one of the prior austenite grains separated by the boundary. The decomposition also occurred within the prior austenite grains, resulting in a Widmanstätten-like morphology. TEM observation showed that this morphology arose from the decomposition of the individual martensite laths.
4. The transition of carbides described above is consistent with the precipitation sequence reported by other investigators. This sequence can be summarized as follows:

$$M_3C \rightarrow M_7C_3 \rightarrow M_{23}C_6.$$
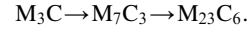
In the present study, the cementite particles dissolved in the very early stages of tempering and were replaced by alloy carbides, M_7C_3 and $M_{23}C_6$. The $M_{23}C_6$ carbides probably nucleated simultaneously with cementite. After tempering times as
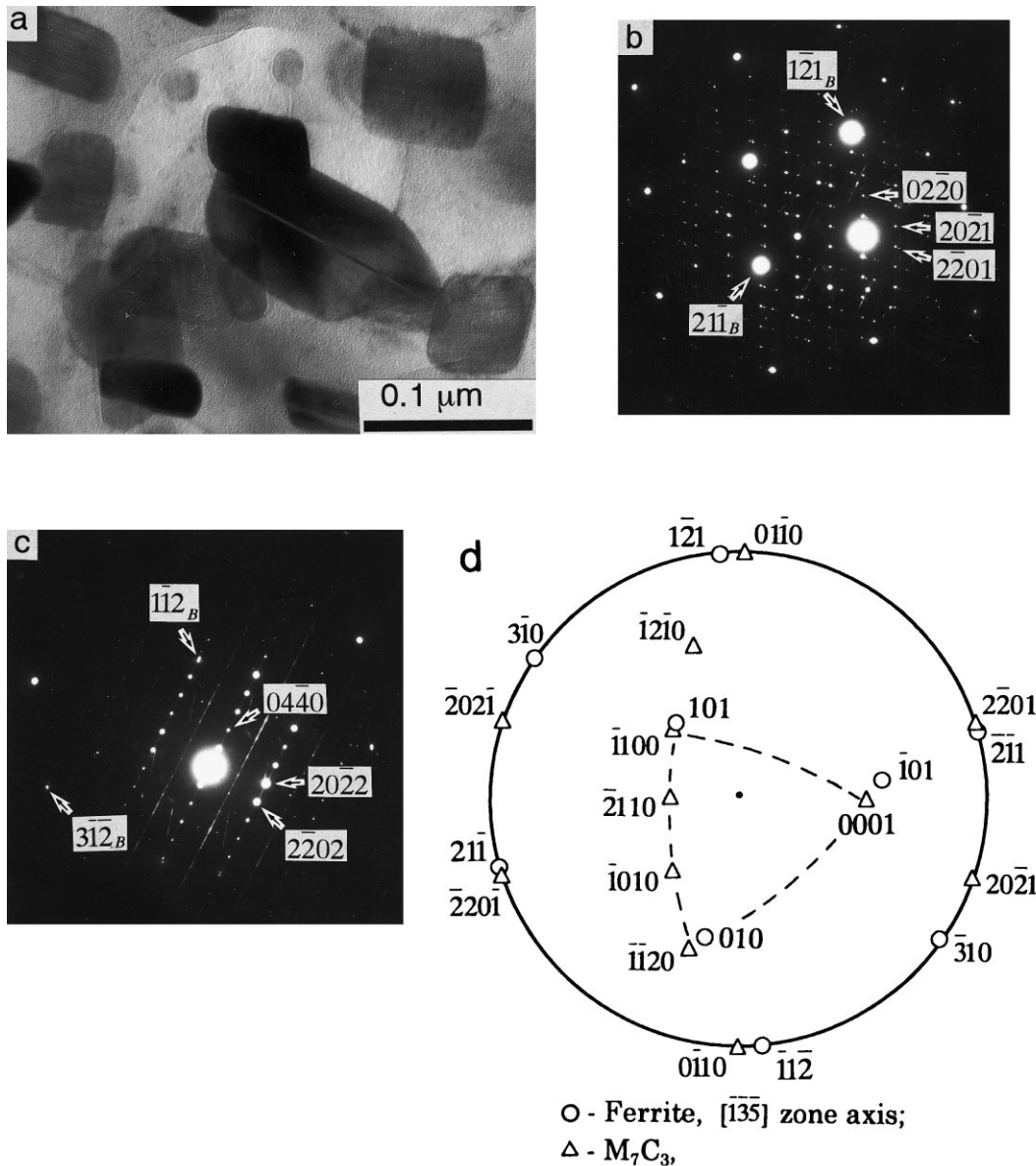
Fig. 14. TEM micrograph showing the M_7C_3 carbide precipitates in the specimen tempered at 735°C for 5 min. (a) Bright field image; (b), (c) SAED patterns taken from different particles at various tilting angles and (d) stereographic analysis for (b).

short as 1 h the M_7C_3 particles were completely replaced by those of $M_{23}C_6$. The morphologies of various carbide precipitates are very similar. As the tempering time is increased, the number of particles per unit volume decreased, and their sizes increased.

4.2. Theoretical consideration

The most important feature of the observed results is the inhomogeneous character of martensite decomposition. The precipitation of cementite particles is much retarded at temperatures as high as 735°C. It can be concluded that with the large amount of chromium in the α' supersaturated solid solution, the driving force for cementite precipi-

tation is much reduced while for alloy carbide precipitation it is increased. Chromium adsorption in the prior austenite grain boundary will reduce the carbon activity, thus, the driving force for carbon diffusion from the bulk martensite towards the prior austenite grain boundary will be obtained. The primary rate-controlling element is carbon when predominant precipitates were cementite. The boundary conditions at the α/M_3C interface is such that cementite inherits the metal composition of the matrix [55], thus the cementite particles grow by a paraequilibrium mechanism. With increasing tempering time, the alloy carbide precipitation at the reaction front becomes controlled by chromium diffusion.

In order to understand the decomposition processes qualitatively it is useful to determine the driving forces for diffusion. The idea that carbon diffusion is governed by activity difference rather than concentration difference was advanced by Darken [56]. Using the thermodynamic equilibrium calculations with the software and database ThermoCalc [57], it is possible to determine the activities at all moving interfaces. Assuming local equilibrium at the moving interfaces, this method has recently been applied to a number of quite complicated reactions in multicomponent systems [58–60] and the experimental results obtained were in good agreement with theory.

Figure 15 shows calculated isothermal sections of the Fe–Cr–C phase diagram at 735°C, representing the four-phase equilibrium between α, M_3C, M_7C_3 and $M_{23}C_6$ with different axes. The other phases were neglected. The dotted lines show the calculated metastable extension of the $\alpha + M_7C_3$ two-phase equilibrium. The filled square denotes the composition of the alloy investigated. The compositions of M_3C, M_7C_3 and $M_{23}C_6$ carbides are represented by stars. The chromium composition of cementite was assumed to be equal to that of martensite. Thomson and Bhadeshia [36] confirmed that $M_{23}C_6$ carbide is close to its equilibrium composition when it starts to form and this result was employed in the present study. Although M_7C_3 carbide may precipitate initially with lower chromium content than $M_{23}C_6$ carbide [24], its chromium composition, to a first approximation, was assumed to be equal to the equilibrium composition. The slanting dashed lines starting from these points define the equilibrium at 735°C between these carbides and the ferrite marked by filled circles. The cross in Fig. 15(b) shows the composition of ferrite without chromium partitioning behind the reaction front. This point is given by intersection between the line of constant chromium content and the line of constant carbon activity. From Fig. 15(b), the carbon activity differences between various interfaces can easily be determined. The driving force for chromium diffusion can be determined using a diagram with chromium activity as one of the axes (see, i.e. Refs [58–60]).
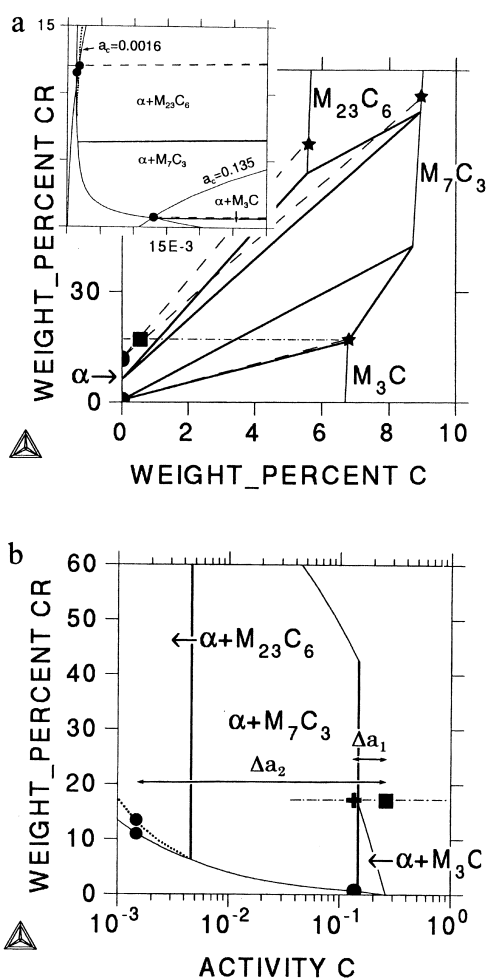
Fig. 15. Calculated isothermal section of the Fe–Cr–C phase diagram at 735°C representing the four-phase equilibrium between α, M_3C, M_7C_3 and $M_{23}C_6$ with (a) weight percent carbon and (b) carbon activity as horizontal axes. The dotted lines show calculated metastable extension of $\alpha + M_7C_3$ two-phase equilibrium. The slanting dashed lines represent the tie-lines of the $\alpha + M_3C$, $\alpha + M_7C_3$ and $\alpha + M_{23}C_6$ equilibria. The composition of alloy is marked by filled square. All the other lines and symbols are explained in Section 4.2.

The possible diffusion directions of carbon and chromium atoms due to the driving forces are shown in Fig. 16 schematically.

When cementite precipitates at the reaction front, the carbon activity difference Δa_1 between the α/M_3C interface and the bulk martensite acts as a driving force for carbon diffusion, see Figs 15(b) and 16(a). Behind the reaction front, the carbon activity in the α matrix approaches the same value as that at the α/M_3C interface [shown by ($\bullet$) and ($+$) in Fig. 15(b)], thus the same driving force exists between the ferrite and the martensite matrix, resulting in further reaction proceeding by autocatalytic nucleation [Fig. 16(a)]. With the diffusion of carbon, there is also a strong driving force for chromium diffusion towards the surface of cementite particles. In this case chromium atoms can be supplied by interface diffusion rather than by volume diffusion. It is well known that the solubility of chromium in cementite is limited. Kuo [25] reported that the maximum solubility is approximately 18 at.%, while Cr contents as high as 21–32 and 40 at.% were measured by Janovec et al. [33] and Karagöz et al. [40], respectively. Thus it can be concluded that in the present 17Cr steel the amount of chromium in cementite will be saturated in an extremely short time in keeping with the results of Robson and Bhadeshia [35]. In order to allow for a lamellar or rod-like cementite growth the flux of carbon toward cementite should be much larger than that of chromium because the growth of supersaturated cementite will slow down and eventually stop or alloy carbides precipitate instead of cementite.

The precipitation of chromium-rich carbides at the reaction front requires the partitioning of chromium. In this case the driving force for carbon diffusion is considerably increased [Δa_2 in Fig. 15(b)] while for chromium diffusion it is decreased. Thus the reaction will proceed by slow diffusion of chromium atoms.

Figure 16(c) shows schematically the possible directions for carbon and chromium diffusion due to the driving forces when all three types of carbides coexist. There are strong driving forces for carbon diffusion away from the α/M_3C interface to the α/M_7C_3 and $\alpha/M_{23}C_6$ interfaces. Thus it is expected that cementite particles will be rapidly dissolved in the vicinity of alloy carbides. If only two alloy carbides coexist, the driving force for chromium diffusion is rather small and it will take much longer time to complete the M_7C_3 carbide dissolution.

4.3. Crystallography

All carbide particles were crystallographically related with respect to the matrix, into which the precipitation occurred. Cementite particles were related to the ferritic matrix with the Bagaryatsky OR. They often precipitated at the reaction front along the martensite lath and twin boundaries resulting in carbide rows. $M_{23}C_6$ carbide was related to ferrite by the Kurdjumov–Sachs OR. Similar OR has been reported by Jung et al. [61] but the OR reported by Kuo and Jia [34] was not found in the present study.

The crystallography of M_7C_3 carbide, however, was found to be much more complicated. Two specific ORs were found to exist between M_7C_3 carbide and ferrite. One of them has previously been reported. Both ORs have the common axis $[0001]_h//[110]_\alpha$. Zhang and Kelly [62–64] suggested that the ORs should be expressed in terms of the edge-to-edge matching model and the present result appears to be in keeping with it. During the crystallographic study of pearlite with M_7C_3 carbide lamellae, however, Shtansky et al. [65] showed that each of the $\{110\}_\alpha$ close packed planes of ferrite is within a few degrees of one of the following planes in the M_7C_3 phase: $\{1\bar{3}22\}_h$, $\{\bar{5}051\}_h$, $\{33\bar{6}1\}_h$, $\{6\bar{2}\bar{4}1\}_h$, $\{73\bar{4}0\}_h$ or $\{10\bar{1}0\}_h$. The d spacings of
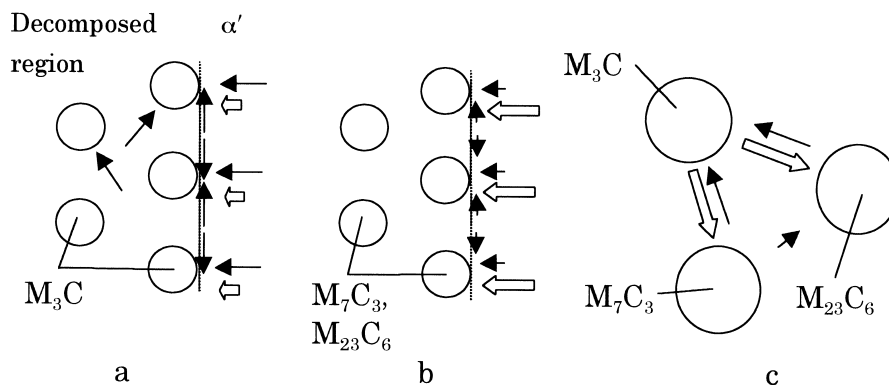

Fig. 16. Possible diffusion directions of carbon (white arrows) and chromium (black arrows) atoms (schematic) as a result of the driving forces which exist when (a), (b) various carbides precipitate at the reaction front and (c) carbides coexist together as the reaction front passes.

these planes are close to that of $\{110\}_\alpha$ ferrite. Thus the rationality of the new OR observed in the present study can be understood considering the stereographic projection in Fig. 17. It can be seen that each of the $\{110\}_\alpha$ close packed planes of ferrite is within a few degrees of one of the following planes in M_7C_3 phase: $\{\bar{5}051\}_h$ or $\{\bar{1}100\}_h$.

The ferrite, which is the decomposition product of martensite and grows into the martensite, inherits its orientation during the decomposition reaction.

4.4. *Transformation mechanism and classification of the reaction*

The martensite decomposition reaction is characterized by the following facts:

1. The decomposition starts at the prior austenite grain boundary heterogeneously with accompanying carbide precipitation on one side of the grain boundary, having a low-energy interface with the martensite in which the reaction proceeds.
2. The reaction is diffusion controlled. The kinetics of martensite decomposition changes from carbon diffusion to chromium diffusion control.
3. The composition of the matrix changes discontinuously as the reaction front passes. No change takes place ahead of the reaction front.
4. There is no grain boundary migration at least at the beginning of the process.
5. The reaction is of autocatalytic type, initiating further nucleation at the reaction front.

▲ - Ferrite, [110] zone axis;
○ - M_7C_3, [0001] zone axis.

Fig. 17. The $[110]_\alpha//[0001]_h$ stereographic projection showing small misorientation between the $\{110\}_\alpha$ ferrite planes and the coincident planes of the M_7C_3 carbide for the new OR.

6. The second phase does not always precipitate as lamellae but as spheroidal or needle-shaped particles along the moving interface having a rational OR with respect to the matrix.

The observed reaction is somewhat similar to a discontinuous precipitation reaction. Although several review papers are available [66–68], there is no rigorous classification of discontinuous precipitation (cellular) reactions. Precipitation that is not cellular is referred to as continuous because it occurs generally throughout the matrix on dislocations or grain boundaries, and the matrix composition at a given point decreases continuously with time [69]. It is obvious that the reaction observed in the present study cannot be identified with continuous type.

The essential characteristic of the discontinuous precipitation reaction is that the composition of the matrix changes discontinuously across the reaction front. According to Type 1 of the reaction nomenclature suggested by Thompson [70] and Williams and Butler [68], a single-phase supersaturated matrix α' transforms behind a moving grain boundary to alternate lamellae of the more thermodynamically stable mixture of β precipitate and solute-depleted α. Other major characteristics of the discontinuous precipitation reaction, which has also been mentioned, are the autocatalytic nature of the reaction, the change of matrix orientation and no third element interaction with the reaction front [67]. In a multicomponent system, however, a more complex type of discontinuous precipitation can occur with two elements becoming rate controlling in an interactive manner [71]. Such an interaction may result in various precipitate morphologies, not only lamellae similar to those observed during the eutectoid reaction of $M_{23}C_6$ carbide decomposition by Shtansky and Inden [58]. They pointed out that, in order to allow for a lamellae or rod-like growth the fluxes of elements which take part in the formation of a second phase must fulfil mass balance conditions. If there are no conditions for the growth of a stable periodic rod-like microstructure, spherical precipitation takes place.

The most important characteristic of the observed reaction which would seem to be different from grain boundary discontinuous precipitation is that, at least at the beginning of the process, the orientation of the matrix is unchanged by decomposition, thus there is no grain-boundary migration as usually realized. The change of the matrix orientation is considered an important factor to produce lattice defects at the reaction front that are able to accelerate nucleation and/or growth of the second phase [68]. It is important to note that in our experiments the sharp interface between the supersaturated solid solution and the decomposed region exists because the dislocation density is quite different on both sides of the reaction front. Moreover, the reaction might proceed with change of the

matrix orientation if the specimen is tempered for sufficient time.

The martensite decomposition reaction is also somewhat similar to some other reactions, which have been discovered in several alloys of α iron, such as Fe–W, Fe–Mo and Fe–Sn [72, 73]. Two specific features of the observed reactions have been noted. The orientation of the matrix is unchanged by decomposition and the shape of precipitates is different from lamellae. These reactions, although having some special features, are sometimes also called discontinuous [73].

In summary, the mechanism, the kinetics and the crystallography of martensite decomposition suggest that the reaction observed can belong to a discontinuous precipitation type. As was pointed out by Williams and Butler [68] the detailed discontinuous reaction characteristics vary tremendously and this conclusion is in keeping with our results.

5. SUMMARY

The mechanism of martensite decomposition, the kinetics of carbide precipitation reaction and their crystallography during tempering at 735°C have been studied in an Fe–17 wt% Cr–0.55 wt% C alloy. The following results were obtained.

1. The martensite decomposed by discontinuous-like precipitation reaction.
2. The decomposition of martensite started preferentially at the initial austenite grain boundaries and occasionally at the martensite lath boundaries and the reaction proceeded by the migration of a reaction front only into one of the adjacent grains.
3. The kinetics of discontinuous-like precipitation reaction changed from carbon diffusion to chromium diffusion controlled with tempering time.
4. The kinetics of carbide transition is quite rapid. Tempering at 735°C for 1 h was sufficient to dissolve all of the transient carbides.
5. The precipitates behind the reaction front were identified as cementite, and/or alloy carbides, $M_{23}C_6$ and M_7C_3. Various carbide morphologies were observed close to the reaction front: rod-like, spherical or lamellae. Each type of carbide had a specific orientation relationship with respect to the matrix and did not depend upon their morphology. Rod-like carbide particles can be oriented in various crystallographic directions. Cementite particles were found to relate to the ferritic matrix via various variants of the Bagaryatsky OR. The $M_{23}C_6$ carbide possessed the Kurdjumov–Sach OR with respect to the ferritic matrix. Two ORs were found to exist between the M_7C_3 carbide particles and the ferritic matrix, both of them had the common axis $[0001]_h//[110]_\alpha$. One of them has previously been reported. It was shown that for the new OR the

misorientation between the close packed planes of ferrite and the coincident planes of M_7C_3 carbide is always within a few degrees. At least at the beginning of tempering, the ferrite inherited the orientation of martensite into which the ferrite grew.

REFERENCES

1. Krauss, G., in *Steels: Heat Treatment and Processing Principles*. ASM International, Materials Park, OH, 1990, p. 218.
2. Speich, G. R. and Leslie, W. C., *Metall. Trans.*, 1972, **3**, 1043.
3. Speich, G. R., *Trans. metall. Soc. A.I.M.E.*, 1969, **245**, 2553.
4. Genin, J. and Flinn, P. A., *Trans. metall. Soc. A.I.M.E.*, 1968, **242**, 1419.
5. Kurdjumov, G. V. and Khachaturyan, A. G., *Metall. Trans.*, 1972, **3**, 1069.
6. Nagakura, S., Hirotsu, Y., Kusuniki, M., Suzuki, T. and Nakamura, Y., *Metall. Trans.*, 1983, **14A**, 1025.
7. Ohmori, Y. and Tamura, I., *Metall. Trans.*, 1992, **23A**, 2147.
8. Jack, K. H., *J. Iron Steel Inst.*, 1951, **169**, 26.
9. Roberts, C. S., Averbach, B. L. and Cohen, M., *Trans. Am. Soc. Metals*, 1953, **45**, 576.
10. Lemeat, B. S., Averbach, B. L. and Cohen, M., *Trans. Am. Soc. Metals*, 1954, **46**, 851.
11. Lemeat, B. S., Averbach, B. L. and Cohen, M., *Trans. Am. Soc. Metals*, 1955, **47**, 291.
12. Hirotsu, Y. and Nagakura, S., *Acta metall.*, 1972, **20**, 645.
13. Hirotsu, Y. and Nagakura, S., *Trans. Japan Inst. Metals*, 1974, **15**, 129.
14. Williamson, D. L., Nakazawa, K. and Krauss, G., *Metall. Trans.*, 1979, **10A**, 1351.
15. Ohmori, Y. and Tamura, I., *Metall. Trans.*, 1992, **23A**, 2737.
16. Balliett, T. A. and Krauss, G., *Metall. Trans.*, 1976, **7A**, 81.
17. Williamson, D. L., Shupmann, R. G., Materkowski, J. P. and Krauss, G., *Metall. Trans.*, 1979, **10A**, 379.
18. Imai, Y., *Trans. Japan Inst. Metals*, 1975, **16**, 721.
19. Ohmori, Y., *Trans. Japan Inst. Metals*, 1972, **13**, 119.
20. Ma, C.-B., Ando, T., Williamson, D. L. and Krauss, G., *Metall. Trans.*, 1983, **14A**, 1033.
21. Nagakura, S., Suzuki, T. and Kusumoki, M., *Trans. Japan Inst. Metals*, 1981, **22**, 699.
22. Caron, R. N. and Krauss, G., *Metall. Trans.*, 1972, **3**, 2381.
23. Honeycombe, R. W. K., *Steels, Microstructure and Properties*. Edward Arnold and American Society for Metals, Metals Park, OH, 1981.
24. Beech, J. and Warrington, D. H., *J. Iron Steel Inst.*, 1966, **204**, 460.
25. Kuo, K., *J. Iron Steel Inst.*, 1953, **173**, 363.
26. Irvine, K. J., Crowe, D. J. and Pickering, F. B., *J. Iron Steel Inst.*, 1960, **195**, 386.
27. Baker, R. G. and Nutting, J., *J. Iron Steel Inst.*, 1959, **192**, 257.

28. Dyson, D. J. and Andrews, K. W., *J. Iron Steel Inst.*, 1969, **207**, 208.
29. Pilling, J. and Ridley, N., *Metall. Trans.*, 1982, **13A**, 557.
30. Saroja, S., Parameswaran, M., Vijayalakshmi, M. and Raghunathan, V. S., *Acta metall.*, 1995, **43**, 2985.
31. Robson, J. D. and Bhadeshia, H. K. D. H., *Mater. Sci. Technol.*, 1997, **13**, 631.
32. Abdel-Latif, A. M. and Corbett, J. M., *Mater. Sci.*, 1982, **16**, 90.
33. Janovec, J., Vyrostkova, A. and Svoboda, M., *Metall. Mater. Trans.*, 1994, **25A**, 267.
34. Kuo, K. H. and Jia, C. L., *Acta metall.*, 1985, **33**, 991.
35. Robson, J. D. and Bhadeshia, H. K. D. H., *Mater. Sci. Technol.*, 1997, **13**, 640.
36. Thomson, R. C. and Bhadeshia, H. K. D. H., *Metall. Trans.*, 1992, **23A**, 1171.
37. Senior, B. A., *Mater. Sci. Engng*, 1988, **103**, 263.
38. Pigrova, G. D., *Metallov. term. Obrab. Metall.*, 1996, **8**, 2.
39. Vitek, J. M. and Kluen, R. L., *Metall. Trans.*, 1983, **14A**, 1047.
40. Karagöz, S., Fischmeister, H. F., Andrén, H.-O. and Cai, G.-J., *Metall. Trans.*, 1992, **23A**, 163.
41. Arbuzov, M. P. and Kurdjumov, G. V., *Zh. tekh. Fiz.*, 1941, **11**, 412.
42. Isaichev, I. V., *Zh. tekh. Fiz.*, 1947, **17**, 835.
43. Bagaryatsky, Yu. A., *Dokl. Akad. Nauk SSSR*, 1950, **73**, 1161.
44. Andrews, K. W., *Acta metall.*, 1963, **11**, 939.
45. Dyson, D. Y. and Andrews, K. W., *J. Iron Steel Inst.*, 1969, **207**, 208.
46. Kurdjumov, G. V. and Sachs, G., *Z. Phys.*, 1930, **64**, 325.
47. Nishiyama, Z., *Sci. Rep. Tohoku Univ.*, 1934, **23**, 637.
48. Wasserman, G., *Arch. EisenhuttWes.*, 1933, **16**, 647.
49. Thomas, G. and Rao, B. V. N., *Proc. Int. Conf. on Martensite Transformation*, Kiev, Naukora (Ukrain), USSR, 1978, p. 57.
50. Thomas, G. and Rao, B. V. N., Report No. LBL-6242, Lawrence Berkley Laboratory, University of California, Berkeley, CA, May 1977.
51. Chilton, J. M., Barton, C. J. and Speich, G. R., *J. Iron Steel Inst.*, 1970, **208**, 184.
52. Speich, G. R. and Swann, P. R., *J. Iron Steel Inst.*, 1965, **203**, 480.
53. Pitsch, W. and Schrader, A., *Arch. EisenhuttWes.*, 1958, **29**, 485.
54. Pitsch, W. and Schrader, A., *Arch. EisenhuttWes.*, 1958, **29**, 715.
55. Shtansky, D. V. and Inden, G., *Acta mater.*, 1997, **45**, 2861.
56. Darken, L. S., *Trans.Am. Inst. Min. Engrs*, 1942, **150**, 157.
57. Hillert, M., in *Proc. Int. Conf. on Solid–Solid Phase Transf.*. TMS–AIME, Warrendale, PA, 1981, p. 789.
58. Shtansky, D. V. and Inden, G., *Acta mater.*, 1997, **45**, 2879.
59. Shtansky, D. V., Nakai, K. and Ohmori, Y., *Z. Metallk.*, 1999, **90**, 25.
60. Shtansky, D. V., Nakai, K. and Ohmori, Y., *Phil. Mag. A*, 1999, **79**, 1655.
61. Jung, Y.-C., Ohtsubo, H., Nakai, K. and Ohmori, Y., *Metall. Trans. JIM*, 1996, **37**, 676.
62. Zhang, M.-X. and Kelly, P. M., *Scripta mater.*, 1997, **37**, 2009.
63. Zhang, M.-X. and Kelly, P. M., *Scripta mater.*, 1997, **37**, 2017.
64. Zhang, M.-X. and Kelly, P. M., *Acta mater.*, 1998, **46**, 4617.
65. Shtansky, D. V., Nakai, K. and Ohmori, Y., *Acta mater.*, 1999, **47**, 1105.
66. Turnbull, D., *Acta metall.*, 1955, **3**, 55.
67. Hornbogen, E., *Metall. Trans.*, 1972, **3**, 2717.
68. Williams, D. B. and Butler, E. P., *Int. Metals Rev.*, 1981, **3**, 153.
69. Porter, D. A. and Easterling, K. E., *Phase Transformations in Metals and Alloys*. Chapman & Hall, London, 1992.
70. Thompson, M. N., Ph.D. thesis, University of Cambridge, 1971.
71. Faulkner, R. G., *Mater. Sci. Technol.*, 1993, **9**, 118.
72. Hornbogen, E., *Z. Metallk.*, 1961, **52**, 47.
73. Predel, B. and Frebel, M., *Metall. Trans.*, 1973, **4**, 243.